Original Research

Magnetic Resonance Imaging and Cochlear Implants: Compatibility and Safety Aspects

Christian Teissl, MS[1] Christian Kremser, PhD[2] Erwin S. Hochmair, PhD,[1] and Ingeborg J. Hochmair-Desoyer, PhD[1]

With cochlear implants, magnetic resonance imaging (MRI) has until recently been contraindicated due to excessive magnetic and electromagnetic interference. The aim of this study was to determine the MRI compatibility of the Med-El Combi 40/40+ cochlear implant, within a wide range of clinical MRI applications. In vitro experiments on a 1.5 T MR scanner were performed. Torque, force, demagnetization, artifacts, induced voltages, and temperature increase were measured in worst case scenarios for the implant. In addition, stabilization experiments were performed. It was shown that most of the electromagnetic interferences between the cochlear implant and the 1.5 T scanner remained within acceptable limits. One exception is the torque on the internal magnet, which represents a hazard for patients with these cochlear implants. Therefore, MRI examination should only be performed if there is a strong medical indication, and certainly some assessment of the relative risks involved versus the risk of not providing the diagnostic capabilities of MRI, will have to be made. Appropriate safety measures should be taken. J. Magn. Reson. Imaging 1999;9:26–38. © 1999 Wiley-Liss, Inc.

Index terms: compatibility; electromagnetic interference; cochlear implant; safety

COCHLEAR IMPLANTS (CIs) are an accepted means of treating profound bilateral deafness by direct electrical stimulation of the auditory nerve. Most of these systems consist of an external, sound-processing device and the actual implant situated in a side-milled-out section of the temporal bone. This implant includes a receiver for the reception of stimulation data via a transcutaneous inductive link, and circuitry for stimulation via electrodes inserted into the inner ear. Small internal CI magnets are used to provide a sufficient transmission quality between the external transmitter and the internal receiver and to hold the external transmitter in place (1).

Around 18,000 implants of various designs are used by adults and children worldwide. Many of these CI wearers will at some point in their life become candidates for magnetic resonance imaging (MRI) examination, a diagnostic tool of rapidly increasing application range. This makes MRI compatibility of CIs an increasingly relevant topic.

The electromagnetic fields appearing during an MRI investigation [static magnetic field, static gradients, switched gradients, radiofrequency (RF) pulses] may interfere with the implant. Eddy currents in conductive elements of the implant could result in heating accompanied by damage to the surrounding tissue or in an induced force during movement. Induced voltages in conductive loops due to RF fields could damage or even destroy the implant (implant-receiver circuit, stimulation electrodes). Force and torque on ferromagnetic parts of the implant due to magnetic field gradients and the homogeneous magnetic field could dislodge the implant, which could result in damage to the implant or the surrounding tissue. Furthermore, the internal CI magnet may cause artifacts in the MR image (2) and could be partially demagnetized, resulting in reduced implant functionality.

Shellock and Curtis (3) summarized the reports of more than 40 publications, concerning the ferromagnetic qualities of 261 different metallic objects on the basis of measurements of deflection forces or attraction during exposure to different static magnetic field strength, ranging from 0.147 to 4.7 T. Applebaum and Valvassori (4) studied 21 stapedectomy prostheses and other middle ear implants, as well as two 22 channel cochlear implant receiver-stimulator modules for ferromagnetism and displacement at 1.5 T. Different studies give a qualitative description of the torque on CIs and other biomedical implants (2,5–8).

Induced signals during MR scans were measured directly via shielded cables and storage oscilloscopes (9), or indirectly by microfuses (2) or full-wave rectified signals (10). These methods have different disadvantages, eg, electromagnetic interference or relatively high detection limits. Furthermore, concerning induced voltages, these studies deal only with specific elements of the implant or with a single interference source (2,9,10). Parameters of the scanner, the RF sequences, or the sample position often do not represent the worst case scenario for the different electromagnetic interferences.

This paper was presented in part at the Fifth Scientific Meeting of the ISMRM, Vancouver, British Columbia, Canada, 1997.

Contract grant sponsor: Austrian Science Foundation; contract grant number: P11755-TEC.

[1]Department of Applied Physics, University of Innsbruck, 6020 Innsbruck, Austria. [2]Department of Magnetic Resonance Imaging, University of Innsbruck, 6020 Innsbruck, Austria.

Address reprint requests to: C.T., Institut für Angewandte Physik, Universität Innsbruck, Technikerstrasse 25, 6020 Innsbruck, Austria.

Received December 29, 1997; Accepted July 14, 1998.

The aim of this study was to determine the MRI compatibility of a CI within the wide range of clinical MRI applications. In vitro experiments on a 1.5 T magnetic resonance scanner (active shielded magnet; Magnetom VISION, Siemens, Germany) were performed. Interference-free measurement techniques were used for the detection of torque, force, demagnetization, artifacts, induced voltages, temperature, and stabilization of the implant using a pressure bandage. RF sequences, RF absorption rates, and geometric positions were varied to determine the worst case scenarios for the implant.

For the present study, the electromagnetic interference between the CI and the MRI scanner was determined. The removable external transmitter and the external speech processor are removed from the patient. Therefore, the patient will be unable to hear during the MRI examination. This inconvenience is outweighed by the benefit of removing additional electromagnetic interference. (For example, the electromagnetic interference between the microphone and the external processor can influence the processed signal, which may lead to overstimulation. The electromagnetic radiation of the external speech processor can interfere with the weak MR signal and affect the signal detected from the MR receiver.)

The CI tested was the multichannel system MedEl Combi40/40+ (MedEl, Innsbruck, Austria), described in Zierhofer et al (11). In this type of CI an amplitude-keyed digital signal is received by a coil (center frequency tuned to 12 MHz; C40 receiver coil: 7 concentrated windings, active total area: 2100 mm^2; C40+ receiver coil: 9 distributed windings, active total area: 2130 mm^2). The plane of the coil is approximately parallel to the skin. Both stimulation information (selection of channel, stimulation pulse length, stimulation pulse level) and supply voltage are derived from the received signal. The demodulated signal is processed by a microprocessor and triggers the current source for stimulation. Excitable tissue in the inner ear is stimulated by current pulses generated by the implant electronics. The stimulating current flows back to the implant via the implanted electrode contacts, the tissue, and the reference electrode. A schematic drawing of the implanted device is shown in Fig. 1.

Small internal magnets (rare-earth permanent magnets of cylindrical shape, magnetized in the main axis of symmetry, which is normal to the skin (remanence: 1.15–1.25 T, coercive electric field intensity: 850–1000 kA/m, energy density 240–310 kJ/m^3) are used to guarantee a sufficient transmission quality between the external transmitter and the internal receiver by holding the external transmitter in place. The macroscopic dynamic behavior of this internal magnet can be described by the magnetic moment, **m** (bold letters designate a vector).

External Magnetic Field

An external magnetic field **B** creates a torque **N** according to

$$\mathbf{N} = \mathbf{m} \times \mathbf{B}, \qquad [1]$$

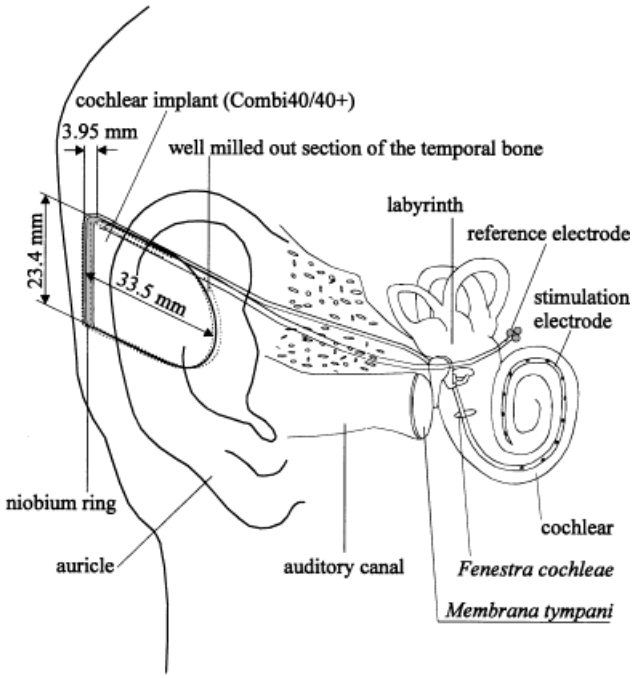

Figure 1. Schematic drawing of the clinical situation of an implanted CI. The implant is placed in a well milled into the temporal bone and fixed with two sutures; then the soft flap over the implant is sutured. The stimulation electrode is inserted into the cochlear, and the reference electrode is placed within the temporal muscle.

Its magnitude N is given by

$$N = m\, B \sin\varphi, \qquad [2]$$

where φ is the angle between **m** and **B**. The strongest torque is experienced in the isocenter of the scanner magnet when the magnetic moment **m** is perpendicular to **B**.

Magnetic Field Gradient

A magnetic field gradient $\nabla\mathbf{B}$ results in an attractive or repulsive force **F** on **m**. The highest values for the attraction (or repulsion) of the internal magnet within an MR scanner occur in the area near the entry into the magnetic bore and near the plastic case of the magnetic bore, where **F** reaches its maximum according to

$$\mathbf{F} = \nabla(\mathbf{mB}). \qquad [3]$$

Demagnetization

Due to the high static magnetic fields of common MRI applications (up to 2 T), the internal magnet can be demagnetized and become too weak to hold the external transmitter in place.

Inhomogeneity

During MR imaging, slice selection and spatial encoding require a strictly homogeneous main magnetic field. The inhomogeneity in the isocenter of commercial scanners

is in the ppm range. The internal CI magnet, representing a magnetic dipole, disturbs the magnetic field homogeneity around its location, resulting in artifacts in the MR images. While signal voids are easy to recognize, distant geometric distortions may be hard to see in common MR images. Knowledge of the area influenced is important to avoid a misinterpretation of MR images due to artifacts.

MATERIALS AND METHODS

All measurements were performed on a 1.5 T scanner using a head or body resonator.

The following experiments were performed with the CI described:

Torque measurements
Force measurements
Evaluation of demagnetization
Evaluation of signal void area and geometric distortion area in MR images
Induced voltage measurements
Temperature measurements
Implant stabilization using a compression bandage

The spatial dependence of the magnetic field within the MR scanner was measured with a magnetic field probe (F.W. Bell, Orlando, FL). From these data, the spatial derivative of the field was calculated and the critical positions of the CI within the scanner concerning the force (maximum spatial derivative) and torque (maximum field strength) were determined.

To detect deflection forces and the torque on the individual elements of the implant during movement into the magnetic field and within the field of the scanner, a method similar to that described by Applebaum and Valvasorri (4) was applied. Implant elements were as follows: implant casing (oxide of aluminum) with niobium ring, header (niobium, gold grommets, ruby-lead-through insulators), stimulation electrode (leads and stimulation lamellas made of a platinum-iridium alloy), reference electrode (platinum-iridium alloy), and substrate (oxide of aluminum) with electronic components. Each element was placed in a transparent plastic box containing a ruler for position measurement. The box was smoothly moved into the magnetic field of the scanner by the transport platform. Any displacement of the CI parts was recorded. Since there was no deflection force and no torque on any of the individual elements of the implant detected, the force and torque measurements were mainly concentrated on the internal magnet of the CI.

Torque Measurement

The internal CI magnet was suspended, almost frictionless, inside a plastic frame, and was constrained to rotate around an axis perpendicular to the main axis of symmetry (Fig. 2). To obtain the maximum value of the resulting torque, and to avoid greater demagnetization, the magnetic moment **m** of the internal CI magnet was kept perpendicular to the magnetic field **B** of the scanner by plastic screws (the deviation from the yz plane

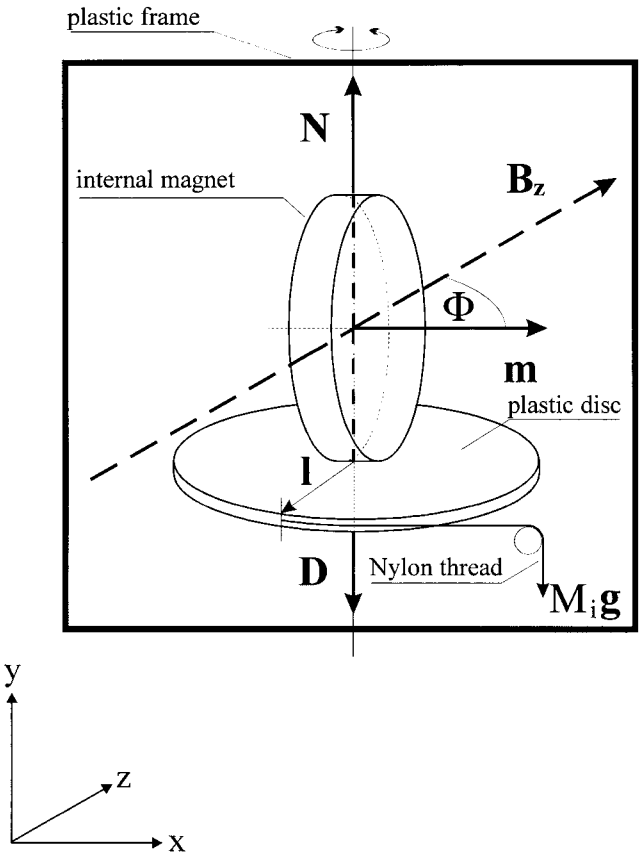

Figure 2. Schematic drawing of the torque measurement. The internal magnet was suspended inside a plastic frame. The deviation from the z axis of the magnet bore was limited to ± 3 degrees to avoid demagnetization. To obtain the maximum value of the torque exerted, the magnetic moment **m** of the internal magnet was kept perpendicular to the magnetic field **B** of the scanner. Plastic weights with the mass M_i were attached to a nylon thread at a position **l** from the pivot, to attain balance between the torque vector **N**, caused by the magnetic field, and the torque **D**, caused by gravitational field **g**.

was limited to ±3°). The small demagnetization that occurred was measured, and the affected torque values were corrected. Plastic weights with the mass M_i were attached to a nylon thread at a position **l** from the pivot, to attain balance between the torque vector **N**, caused by the magnetic field, and the torque **D**, caused by gravitational field **g**. When balance exists between **N** and **D**, the unknown vector **N** is equal to **D** if neglecting friction N and can be found by

$$\mathbf{N} = \mathbf{D} = M\,\mathbf{g} \times \mathbf{l},\ (M = \Sigma M_i). \qquad [4]$$

Force Measurement

The measurement of the longitudinal force F_{Bz} was performed along the rotational symmetry axis of the bore ($\delta B_r/\delta r = 0$) with the magnetic moment **m** of the internal CI magnet aligned with the main magnetic field. As long as **m** is oriented parallel to the applied field, no change in magnetization occurs since the magnetization of the rare earth permanent magnet used is saturated. Furthermore, no rotational forces acting on the

internal CI magnet exist, and therefore an almost frictionless suspension was easily realized by suspending the CI magnet inside a plastic frame using two nylon threads. Inside the plastic frame the internal CI magnet was constrained to rotate around an axis perpendicular to the main axis of symmetry, on the end of a fiberglass pole (Fig. 3). In this configuration, the method is similar to that of New et al (12), in which the force measurement is transformed into an angle measurement. To compensate for the mass of the plastic frame and the pole, a plastic cylinder on the opposite side was adjusted in such a way that only the mass of the small magnet produced an opposing force as the magnet was lifted up by an attractive force. Otherwise the determination of the opposing force would be difficult. The deflection angle was measured with a protractor. Plastic weights were added to keep the deflection angle between 25° and 65° to minimize percentage errors (5). The force components were measured along the z axis of the bore. With

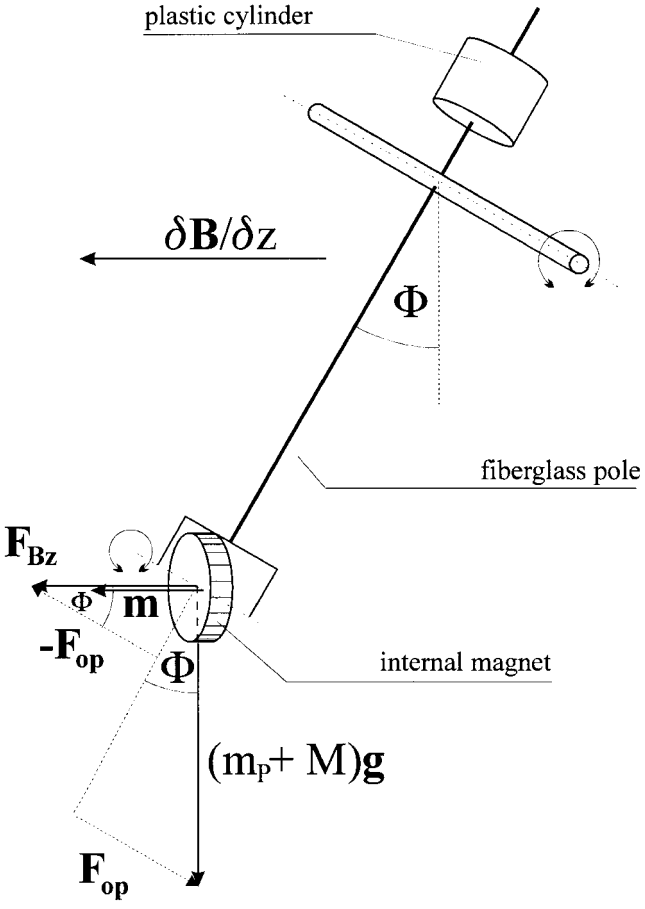

Figure 3. Schematic drawing of the force measurement. The internal magnet was suspended inside a plastic frame and constrained to rotate around an axis perpendicular to the main axis of symmetry, on the end of a fiberglass pole. To compensate for the mass of the plastic frame and the pole, a plastic cylinder on the opposite side was adjusted accordingly. The force component F_{Bz} was detected along the z axis of the bore [determined from the gravitational component $F_G = (m_P + M)g$ and the deflection angle Θ]. m_P = mass of the internal magnet, M = added mass for minimal percentage error, g = gravitational constant, $\mathbf{F}_{op}$ = opposing force due to m_p and M.

the measured deflection angle measured Θ, the force component F_{Bz} perpendicular to the gravitation force component F_G was determined by

$$F_{Bz} = (m_P + M)g \tan\Phi, \quad [5]$$

where m_P is the mass of the internal magnet, M the added mass for minimal percentage error, and g the gravitational constant.

The gradient of the main magnetic field $\delta B_z/\delta z$ was measured at the same locations as for the longitudinal force measurement with a magnetic field probe. From this the longitudinal force component was calculated and compared with the experimental result.

In addition, the gradient of the radial field component $\delta B_r/\delta r$ was measured at the entry of the MR magnet, representing the worst case for the radial derivative of B_r. With these data, the radial force component on the internal CI magnet (F_r), with **m** in radial direction, was calculated.

Demagnetization

The magnetic field intensity $\mathbf{B}_{intmag}$ from the internal CI magnet was detected by Hall measurement before ($\mathbf{B}_{intmag1}$) and after ($\mathbf{B}_{intmag2}$) moving the internal magnet 1 and 10 times into and out of the main magnetic field. The internal magnet was fastened on a plastic mounting in the center line of the main magnetic field. The following orientations of **m** to the z axis were investigated: **m** in the x-direction (usual head position), **m** in the y-direction (head turned 90° to the side), **m** parallel and antiparallel (worst case) to z. Since the total duration of a typical MR investigation is 45 minutes, all demagnetization studies on the internal CI magnets were performed for this length of time. For each measurement a new magnet was used.

Areas of Signal Void and Geometric Distortion

For the determination of image artifacts produced by the internal magnet of the CI, two different experiments were performed.

In the first experiment, we determined the influence of the magnetic field inhomogeneity due to the magnetic field of the internal CI magnet on slice selection. A micro-testplate forming a two-dimensional grid-like structure was filled with a 2 mm thin layer of contrast medium solution (0.0001 mmol/mL of gadolinium-diethylene-triamine-pentaacetic acid; Omniscan, Nycomed, Norway). This thin layer of fluid, corresponding to a coronal orientation, was imaged within the MR scanner. To facilitate transmitter and receiver adjustment for the MR imaging experiment with this small fluid volume, bottles filled with 1500 mL of water were placed near the micro-testplate to permit adjustment. The internal magnet was fastened to the plate with **m** in the x-direction of the scanner magnet (usual head position). This arrangement was put into a load-phantom and positioned in the center of the head coil. Multislice two-dimensional spin-echo sequences (TR 1500 msec, TE 15 msec, coronal, receiver bandwidth 130 Hz/pixel) were used for image acquisition. Any

signal detected in coronal planes different from that corresponding to the fluid layer (k = ± n, n = 1, 2,...) must originate from the fluid plane. Thus the displacement of each grid point due to the slice excitation can be reconstructed (the x and z coordinates from the displaced point were identified with the help of the grid, and y by y = n × d, d = distance of the coronal slices).

In the second experiment, a stack of seven conventional micro-testplates (96-well of rectangular cross section) filled with water was used. It was placed in the load-phantom and positioned in the center of the head coil. The internal CI magnet was fastened to the lowest plate with **m** in the x-direction of the scanner magnet. Multislice two-dimensional spin-echo sequences (TR 1500 msec, TE 15 msec, coronal, receiver bandwidth 130 Hz/pixel) were used for image acquisition, before and after adding the internal magnet.

A vector $\mathbf{v_i}$ was assigned to each well i (Fig. 4) to determine its original position. Adding the internal magnet, the new position $\mathbf{v_i'}$ of each well i was determined and the difference vector **(vi** = **vi**-**vi**′), a measure for the distortion due to the field inhomogeneity, was calculated. The x and z components of each vector $\mathbf{v_i'}$ (of well i) could be determined by the projection of well i in the coronal plane k, and the y component could be calculated by y = k × d. A specific region was called a void if this area showed a pronounced contrast reduction (50% signal reduction per pixel) in comparison with undisturbed areas of the image.

Induced Voltage Measurement

The induced voltage was measured for different worst case sequences at the parallel resonant circuit of the implant receiver (center frequency 12 MHz, capacitance 73.6 pF, inductance 2.39 µH) between P1 and P2 as indicated in Fig. 5a, by a specially designed, electro-optical transducer (Fig. 5b). Between these two points, the maximum allowed peak voltage (6 V) is well known. The impedance of the electro-optical transducer was comparable to the input impedance of the implant, which was important to maintain the quality of the parallel resonant circuit. The electro-optical transducer was shielded by an aluminum box. The RF signal induced was rectified by an RF diode and filtered by a low-pass filter. This demodulated signal fed a biased fiberoptic transmitter diode. The optical signal was transmitted outside the RF cabin via an optical fiber to an optical detector, where it was amplified and displayed by a digital storage oscilloscope (Fig. 5c).

The noise level at the optical detector output was about 4 mV_{pp}, mainly due to the fiberoptic photodiode of the optical detector. Therefore, the minimum detectable signal at the optical detector output was 2 mV peak, which corresponded to 20 mV_{pp} of measured induced RF signal. The critical range for induced voltages of the tested CI was at 6 V peak; therefore the resolution of the measurement setup was far beyond the required resolution. The signal-to-noise ratio (SNR) for the measurements described was 18 dB, which offers a satisfying accuracy of the induced voltage; the time resolution was 5 µsec.

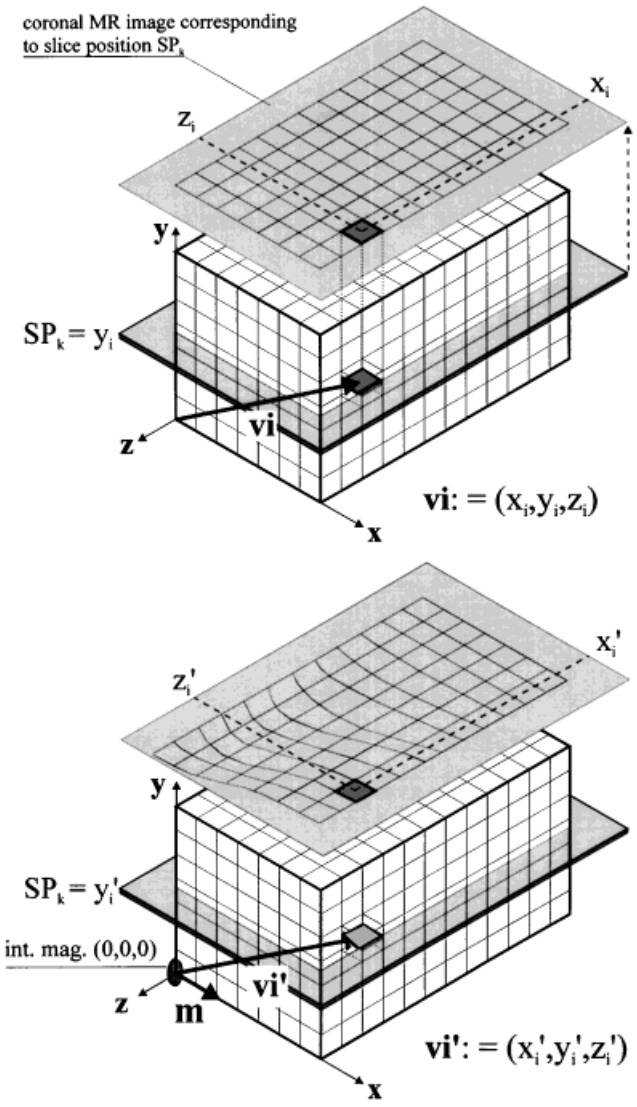

Figure 4. Schematic drawing of the three-dimensional signal void/distortion setup. Seven conventional micro-testplates were stacked one on top of the other to get a periodic structure of water-filled wells. Vectors $\mathbf{v_i}$ (x_i,y_i,z_i) were assigned to each well to determine its original position. Adding the internal magnet (position 0,0,0) with **m** in normal patient orientation, the new positions $\mathbf{v_i'}$ of each well were determined. Then the difference-vectors **(vi** = **vi** - **vi**′), a measure for the distortion due to the field inhomogeneity, were calculated. The components x, x′, z and z′ of each vector $\mathbf{v_i'}$ could be determined by its position in the corresponding coronal MR image; the y and y′ components could be calculated by y = k × d, where d is the distance between coronal slices and k the index of the corresponding coronal slice SP_k.

Without an input signal, the bias current of 0.2 mA led to a direct voltage at the optical-detector output, a measure for the optical coupling between the electro-optical transducer and the optical detector. This direct voltage and the terminal voltage of the electro-optical transducer were used for calibration of the measurement setup, permitting absolute voltage measurements.

To determine the influence of the electromagnetic fields of the MR scanner on the measurement system,

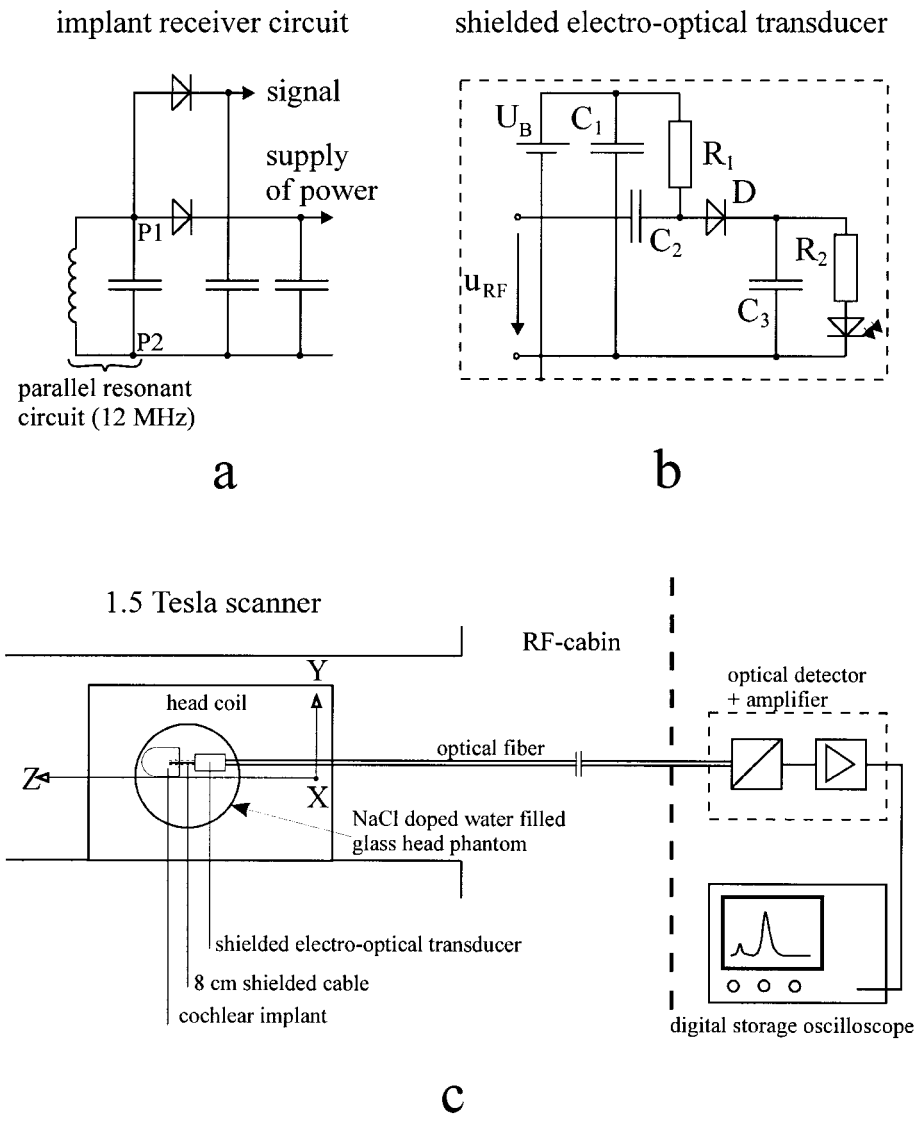

Figure 5. a: The induced voltage was measured between the points P1 and P2 at the implant receiver parallel resonant circuit (center frequency 12 MHz) by a shielded electro-optical transducer. The implant orientation was the same as in a patient during an MRI scan (sagittal, coronal). **b:** Circuit diagram of the shielded electro-optical transducer. The induced radiofrequency signal u_{RF} in the implant receiver circuit is rectified by a Schottky-diode D and filtered by a low-pass filter. This demodulated signal is fed to a biased LED. The electro-optical transducer is shielded by an aluminum box. C_i = capacitors, R_i = resistors, U_B = supply voltage. **c:** Arrangement for the measurement of the induced voltage. The optical signal is transmitted to a photodetector via an optical fiber. The detected signal is amplified and displayed by a storage oscilloscope.

the surface of the receiver coil was rotated into the transversal plane. The position of the electro-optical transducer remained unchanged. Since the magnetic field vector of the RF signal is polarized in the transversal plane, nearly no signal is to be expected with this coil orientation. Thus any signal measured must be induced in the electro-optical transducer itself. These residual signals were found to be below 5% of the signal at the input of the electro-optical transducer.

To simulate different RF load situations, a water-filled glass head-phantom doped with NaCl was put into the head coil. With this phantom, it was also possible to simulate the off-center position of the implant just below the skin. The transmitter reference amplitude U_{TRA}, as determined by the MRI scanner, was used to adjust the NaCl concentration for proper RF peak absorption. Normal U_{TRA} values were determined with the help of eight female and male volunteers of different weights and body sizes.

Sequences containing pulses with high RF peak amplitudes (180° pulses in spin-echo sequences, pulse trains of very short 180° pulses in fast spin-echo sequences) and sequences containing saturation pulses and adiabatic inversion pulses were used to detect the maximum induced peak voltage at the receiver parallel resonant circuit. The implant orientation was as in a real patient situation during an MRI scan (sagittal, coronal). Since the RF signal is polarized in the transversal plane, this is the worst case orientation, giving the largest induced voltage, because the magnetic field vector of the RF is perpendicular to the surface of the coil.

The induced voltage in the stimulation electrode-reference electrode loop was measured during spin-echo and fast spin-echo sequences. The plane of the loop formed by the electrodes was sagittal, which was the worst case orientation. The area of the loop was equivalent to a clinical situation, and the tissue impedance was simulated using a physiological NaCl solution. Both head and body resonator were used for RF transmission.

The implant was tested for functionality after running different worst case sequences.

Temperature Measurement

The implant was fixed in the usual patient orientation on the glass head-phantom filled with a 0.9% NaCl

solution. The surface temperature of the niobium ring (which is part of the seal of the ceramic implant package) was measured without a surrounding conductive medium since the induced eddy currents are mainly determined by the low resistance of the niobium ring.

The temperature measurement at the reference electrode–tissue junction was carried out with a functioning implant; the reference electrode and the stimulation electrode were imbedded in a piece of fresh meat. The low-frequency electrode impedances for all channels were determined by telemetering measurements, as usually used during surgery and postoperative checkups. The impedances determined in our setup were similar to typical impedances measured in patients after implantation.

To minimize the influence of the temperature sensor on the sample, a commercial remote temperature sensor was used [Luxtron remote phosphor kit (13)]. Thin layers of phosphorus material were placed on different spots of the niobium ring and on the contact of the reference electrode. The fluorescence signal of this phosphorus material has a variable decay time dependent on the ambient temperature. This signal was transmitted outside the RF cabin via an optical fiber to the control unit. This contactless temperature sensing permits a minimum of thermal interference, which was important for samples with small thermal capacity (eg, the reference electrode). The temperature during repeated fast spin-echo and half-Fourier single-shot turbo spin-echo (HASTE) sequences was measured by a Luxtron model 710 fluoroptic thermometer (13), calibrated following the procedures described in the Luxtron operator's guide. (The reference temperature was provided by a constant temperature bath.) TR, echo spacing, and number of slices were selected to get high specific absorption rate (SAR) levels corresponding to the "first level operating mode" (14).

Stabilization Experiment

To simulate the actual situation of the implanted CI, which is not adequately sutured to the bone, an implant was placed in a side-milled-out section of a piece of plastic. The piece of plastic was located on a plastic tube with the diameter of an average human head. Crosshairs were reflected by a little mirror mounted at the side of the implant intended to face toward the skull and projected on a viewing screen with a millimeter scale. Since in the real clinical situation the milled well makes a transposition unlikely and the rotation plane is known, the deflection angle could be assigned uniquely to the orientation of the implant within the field. The C40+ implant has a thickness of 4 mm (6 mm for the C40 implant); the well depth varies, but is at least about 2 mm. For the stabilization experiment, the well depth was 3 mm. To simulate the soft flap of skin above the implant, a 3 mm thick piece of pressed sausage meat was used. Stabilization was attained by using a compression bandage (5 m stretched, 2.9 m nonstretched, 8 cm wide) and a hard rubber cube (two erasers held together by a mull bandage; dimensions: 40 × 22 × 22 mm). The deflection angle of the stabilized implant was measured at the isocenter of the scanner (Fig. 6).

RESULTS

Torque Measurement

The torque on the internal CI magnet as a function of the distance from the isocenter is shown in Fig. 7. The maximum torque was detected within the isocenter (N = 0.17464 Nm ± 0.0073), **m** perpendicular to $\mathbf{B_Z}$ (usual head orientation). The mean magnetic moment $<\mathbf{m}>$ = 0.11691 Nm/T ± 0.0057 of this internal magnet was calculated given the measured torque and the measured magnetic field component $\mathbf{B_Z}$.

Force Measurement

No movement of any element (implant casing with niobium ring, header, stimulation electrode, reference electrode, substrate with electronic components) was detected when the parts were brought into the magnetic field of the scanner.

The maximum horizontal force component F_z on the internal CI magnet was 0.3 N at 950 mm distance from the isocenter (Fig. 8), with **m** parallel to $\mathbf{B_Z}$. The correla-

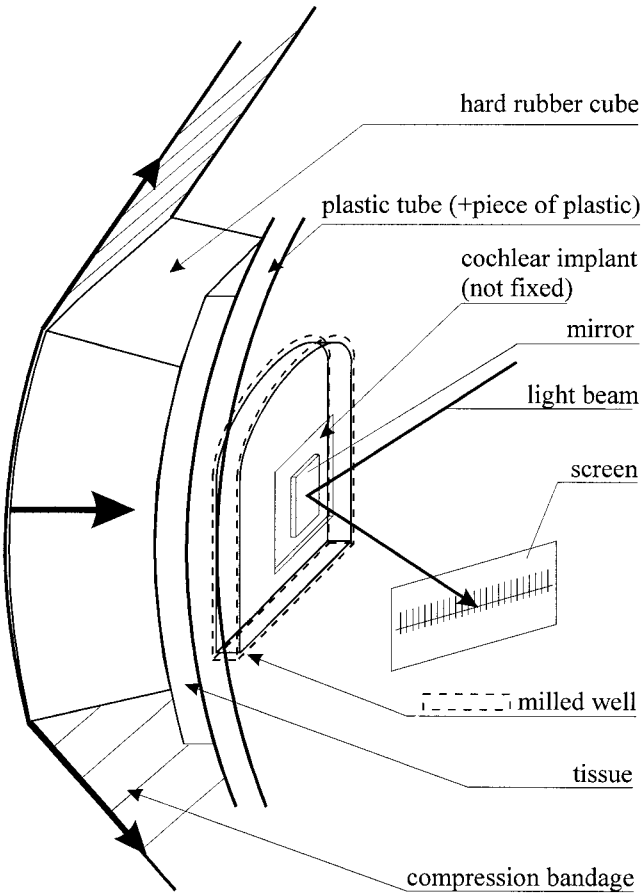

Figure 6. For the stabilization experiment, the actual situation of the implanted CI was simulated. The implant was placed in a well milled in a plastic tube. Crosshairs were reflected by a mirror mounted at the side of the implant intended to face toward the skull and projected on a screen with a millimeter scale. A piece of tissue was used to simulate the soft flap over the implant. Stabilization was attained by using a compression bandage and a hard rubber cube. The deflection angle of the implant was measured in the isocenter of the scanner.

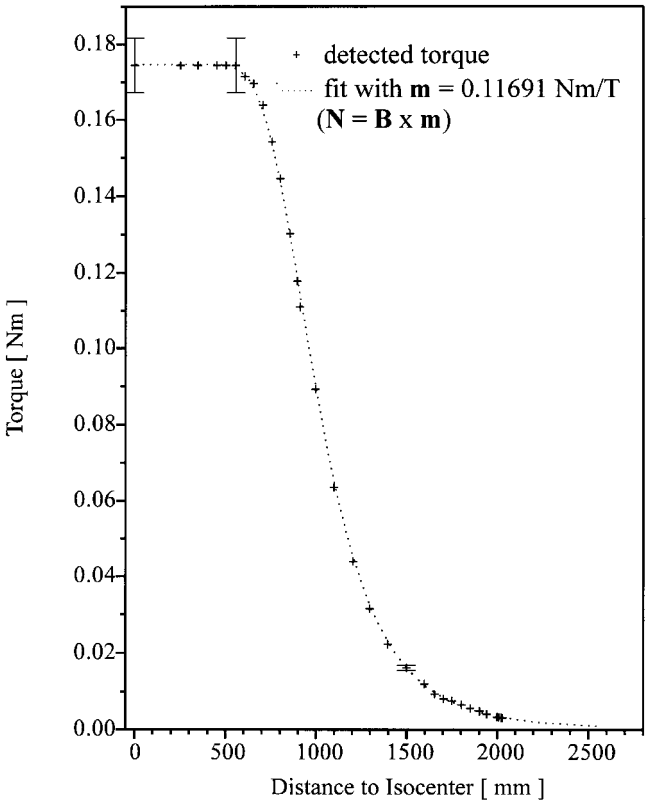

Figure 7. The torque exerted on the internal magnet as a function of the distance to the isocenter (cross +) with the magnetic moment m perpendicular to B_z (usual head position). The dotted line represents a curve fitted using the measured magnetic field of the imager and m = 0.11691 Nm/T.

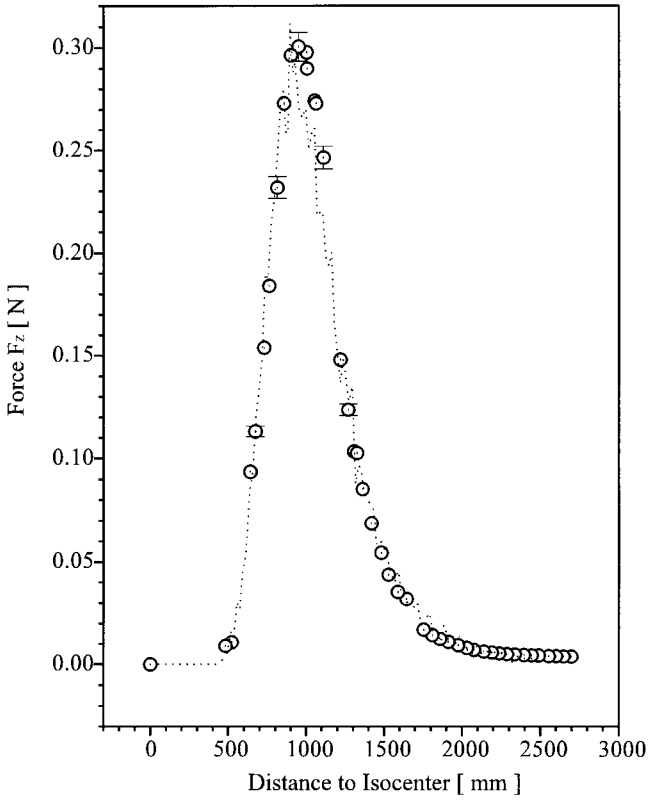

Figure 8. The horizontal force component F_{Bz} on the internal magnet as a function of the distance to the isocenter (circles). The dotted line represents the calculated force m dB/dz.

tion of the measured force and the force predicted by the measured magnetic field gradients is also shown in Fig. 8.

The maximum radial force component F_r on the internal CI magnet was 0.42 N at 871 mm distance from the isocenter, **m** in the radial direction, 10 mm from the plastic cover of the magnet bore. In the usual head orientation the maximum radial force component F_r on the internal CI magnet during movement into the isocenter was 0.17 N.

Demagnetization

The demagnetization of the internal CI magnet results in a magnetic field decrease of 38.3% ± 0.7% in the worst case orientation (**m** antiparallel to B_Z). No difference between 1 time exposure and 10 times exposure to the MRI field was measured. No demagnetization was detected in the usual head orientation after 10 consecutive exposures to the main magnetic field.

Areas of Signal Void and Geometric Distortion

Figure 9 shows the analyzed MRI image of a two-dimensional periodic structure in the coronal plane without (Fig. 9a) and with (Fig. 9b) an additional internal CI magnet (**m** in the x-direction) for spin-echo sequences. The blank space was due to signal voids. The deviation of the original coronal plane had a maximum y-component of ± 5 mm. Since each grid point in the second artifact experiment was separated by 10 mm in the y-direction, the influence on slice selection was avoided by positioning coronal slices in the middle of each micro-testplate.

The results of the artifact measurement using a stack of micro-testplates are summarized in Table 1. There was no geometric distortion in the phase encoding direction (x-axis).

Induced Voltage Measurement

The transmitter reference amplitude-voltage U_{TRA} is a reference for the RF load. It is obtained from the MRI scanner. The U_{TRA} for eight adult volunteers were between 57 V and 74 V, depending on the RF absorption cross section of the volunteer's head. The U_{TRA} is shown as a function of the NaCl concentration of the head-phantom in Fig. 10.

The induced peak-to-peak voltage during spin-echo sequences at the parallel resonant circuit of the digital Combi 40 implant is shown in Fig. 10 as a function of the NaCl concentration. The maximum induced voltage was 1.51 V_{pp} at a NaCl concentration of 0.9 % (U_{TRA} = 71.1 V) and was nearly constant up to an NaCl concentration level of 2.24 % (U_{TRA} = 106.9 V). The induced voltage at the parallel resonant circuit of the implant during the use of adiabatic inversion pulses and saturation pulses was below the induced voltage due to the 180° spin-echo pulses. The worst case for the induced voltage was found to be for fast spin-echo sequences

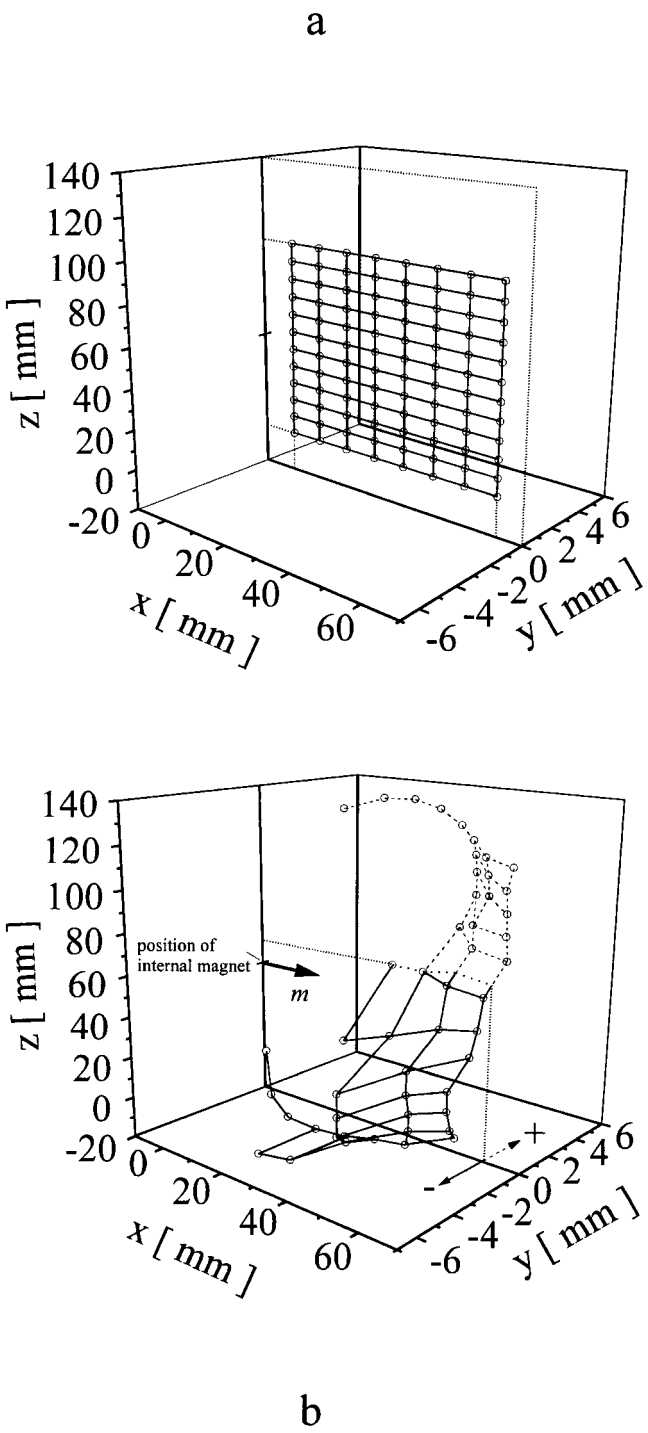

Figure 9. a: The periodic structure of a two-dimensional layer (12 × 8 wells of rectangular cross section, filled with 2 mm contrast medium solution) in the MRI scanner (main magnetic field in z-direction). The points represent the x, y, and z coordinates of the data of the periodic structure obtained from the MR image. **b:** After adding the internal magnet with the magnetic moment **m**, the coronal, sagittal, and transversal layers were compared with a. Using this information, the distortion of the periodic structure was determined. Note the different scale on the y axis.

with short pulse duration, where the induced voltage had a maximum of 2.12 V_{pp}.

The maximum induced voltage during spin-echo sequences in the loop formed by the stimulation electrode and the reference electrode was 6.05 V_{pp} (area of the loop 2100 mm^2).

There was no difference between using the head or the body resonator for RF transmission. The induced signal due to switched gradients for worst case sequences (echoplanar imaging), sequence parameters, positions, and orientations was negligible.

Table 1
Geometric Distortion and Signal Void Limit Due to the Internal Magnet*

Artifact (mm)	Distance to the internal magnet (mm)
$\Delta vi_z \geq$	
0.35 ± 0.19	140.5 ± 3.2
1.00 ± 0.19	124.2 ± 3.2
4.00 ± 0.19	76.50 ± 3.2
$\Delta vi_x \geq$	
0.0 ± 0.19	140.5 ± 3.2
0.00 ± 0.19	124.2 ± 3.2
0.00 ± 0.19	76.50 ± 3.2
Signal void	44.50 ± 3.2

*Δvi_z = geometric distortion in the z-direction (frequency encoding direction); Δvi_x = geometric distortion in the x-direction (phase-encoding direction).

Temperature Measurement

The results of the temperature measurements are summarized in Table 2. The maximum detected surface temperature increase of the niobium ring was 0.1°C ± 0.1°C during continuous HASTE sequences (TR 10.92 msec, TE 87 msec, number of slices 13). The maximum measured temperature increase at the reference electrode-tissue junction was 0.4°C ± 0.1°C, using continuously repeated HASTE sequences and the same worst case parameters (Fig. 11).

Stabilization Experiment

Using a compression bandage and a hard rubber cube for stabilization, the deflection angle of the implant due to the torque on the internal magnet was 2.7° ± 1.0°. The deflection angle using only a compression bandage wound around the head was 17° ± 1.0°.

DISCUSSION

It was the aim of the study to define the present state of MRI compatibility of the CI described, which is important for patients wearing this type of implant. The 1.5 T system was selected for this study since it offers some worst case scenarios (high mean and peak transmitter RF power, active shielded magnet with a high spatial derivative of the field, high static magnetic field). The MR unit used permitted a broad spectra of RF sequences and high values for the gradient field strength, as well as short rise and fall times. The longitudinal main magnetic field orientation and the transversal RF field orientation represent worst case orientations for torque, induced voltage, and temperature increase. Commercially available open MR systems with transversal field orientation represent no additional interfer-

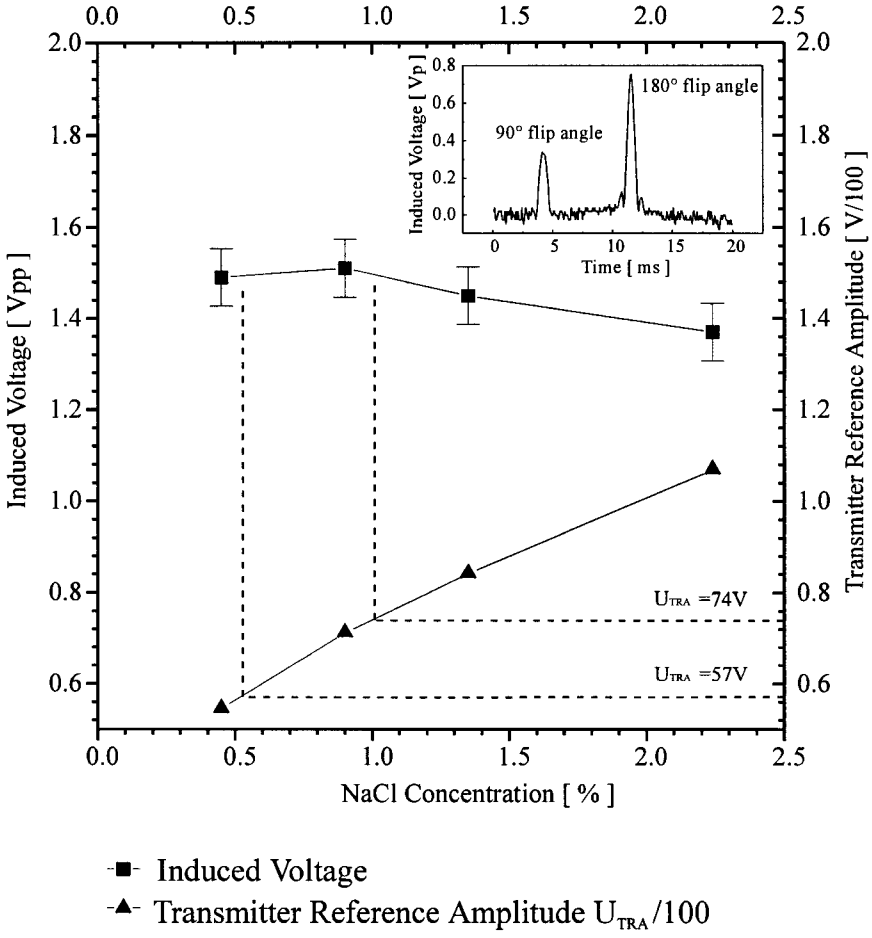

Figure 10. The maximum induced peak voltage during SE sequences at the receiver circuit from the Combi40 (Combi40+) implant, detected by an electro-optical transducer (filled squares). The filled triangles represent the transmitter reference amplitude voltage (U_{TRA}) as a function of the NaCl concentration of the head phantom. The insert shows the rectified SE-RF pulses. The setup was calibrated outside the RF cabin with RF pulses of known amplitude, which enabled absolute voltage measurements owing to the relation between the output signal and the RF voltage at the input of the electro-optical transducer.

ence; however, no direct conclusion concerning transverse field systems can be drawn.

Demagnetization

Demagnetization of the internal CI magnet can be avoided by taking care to orient the head of the patient properly near and inside the MR magnet. Since there is no demagnetization in the usual head position, the head should be oriented parallel to the magnetic field of the scanner. For commercial open MR systems with transversal main magnetic fields and a lower main magnetic field strength, the demagnetization can be neglected due to the high coercive electric field intensity of the rare-earth permanent magnets used in this type of CI.

Artifacts

Although there were artifacts due to the receiver coil and the electrodes of the CI, the primary reduction in image quality was due to the internal magnet. The area influenced can be slightly improved by choosing proper RF sequences.

Induced Voltage

Maximum induced voltage levels were given by the manufacturer. For the CI receiver parallel resonant circuit and the loop formed by the stimulation electrode, tissue, reference electrode, and CI, the maximum allowed input voltages were 6 V peak. The induced peak

Table 2
Temperature Increase for Different Implant Elements and Worst Case Sequences*

Sequence	TR (msec)	TE (msec)	NoSl	tSeq (sec)	Sample	ΔT (°C)
SE	300	15	10	160	Niob. ring	0.0
Fast SE (tse)	2000	128	5	216	Niob. ring	0.0
Fast SE (HASTE)	10.92	87	13	174	Niob. ring	0.1
Fast SE (tse)	2000	128	5	220	Reference el.	0.4
Fast SE (HASTE)	10.92	87	13	260	Reference el.	0.3
Fast SE (HASTE)	8.2	66	21	176	Reference el.	0.4
Fast SE (HASTE)	8.2	66	13	650	Reference el.	0.4

*NoSl = number of slices; tSeq = total period of the continuously repeated sequences; ΔT = temperature increase of sample; tse = turbo spin echo; HASTE: = half-Fourier single-shot turbo spin echo; Niob. ring = niobium ring; Reference el. = reference electrode.

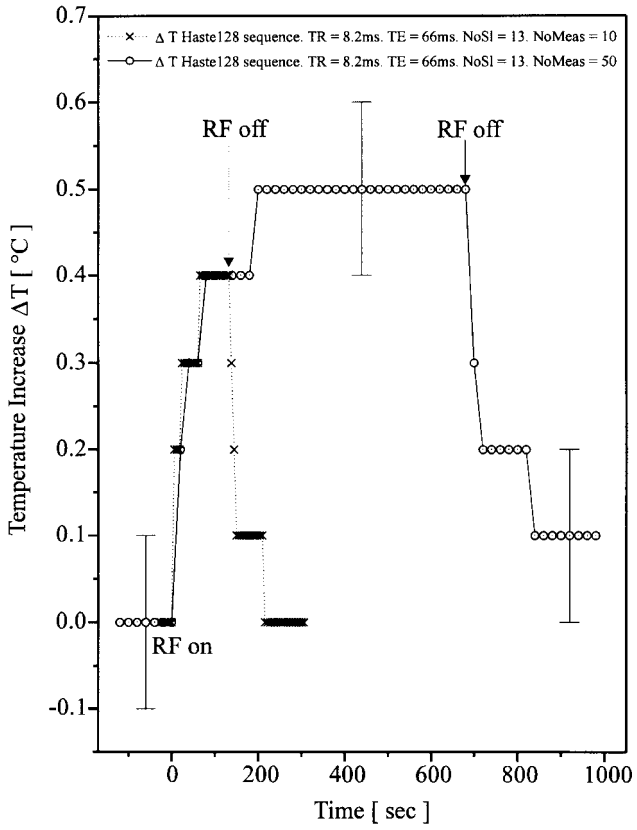

Figure 11. Temperature increase detected by a Fluoroptic temperature measurement system at the electrode-tissue junction during continuously repeated fast SE sequences for different examination durations.

voltage in the parallel resonant circuit of the receiver of the Combi 40 (Combi 40+) implant during spin-echo sequences, fast spin-echo sequences, and sequences containing adiabatic inversion pulses, saturation pulses, or non-slice-selective RF pulses was below this maximum allowed input voltage. Also the induced peak voltage in the loop formed by the electrodes during spin-echo equences and fast spin-echo sequences was below this limit. There was no significant difference between using the head coil or the body coil for RF transmission.

Other MR scanners may generate shorter RF pulses, which produce higher amplitudes, leading to a destruction of the implant. In addition it should be stated that the induced voltage in the implant receiver circuit may increase with *decreasing* static magnetic field, since the affiliated MRI frequency gets closer to the transmission CI carrier frequency of 12 MHz.

The maximum currents delivered by the CI are limited by the implant circuitry to avoid physiological damage. However, an uncomfortable loudness sensation in the event of destruction of the implant circuitry is possible. Because all induced voltages remained within the limits set by the manufacturer under the parameters tested, and performance tests after worst case sequences showed no influence on the functionality of a CI studied, we can exclude this possible scenario.

By varying the NaCl concentration in the H_2O head phantom, it was possible to simulate different RF loads. As shown in Fig. 10, the induced peak voltage stays nearly constant as the RF load increases when the NaCl concentration is increased. From that we conclude that there will be no significant increase in the induced peak voltage with patients of different head sizes.

The data transmission from the external transmitter to the implanted receiver of the Combi 40 and Combi40+ implant uses a digital format with error detection (11). Because the risk of electromagnetic interference occurs in many situations in everyday life, exhaustive reliability tests of the error detection software were made during the development of the implant. RF-induced voltages during an MR scan do not generate a pulse format similar to the digital format used by the Combi 40 and Combi40+ implants to trigger a stimulation signal. Therefore, no accidental undesired stimulation during RF sequences is likely to occur.

Temperature Measurement

The temperature was detected at the niobium ring and the reference electrode. The remaining parts of the implant are of limited consequence. (The implant housing is made of ceramic, and the reference electrodes, the stimulation electrode, and the header are isolated with a silicone coating.) Since the surface-current density at the reference electrode-tissue junction is comparable to the surface-current density at a single stimulation electrode lamella, the temperature was only detected at the reference electrode. Heating of the different components of the implant is determined by the mean temporal RF power distribution of the RF sequence (SAR), fast spin-echo sequences containing high repetition rates of series of 180° pulses were therefore used. The maximum detected temperature rise was below the Food and Drug Administration limit for maximum allowable temperature increase of 1.0°C in the head region during MRI (16). Nevertheless, a temperature increase could be prevented by selecting sequences with a low average RF power.

Torque and Force Measurement and Stabilization Experiment

For the patient's comfort and safety, force and torque on the CI should be as low as possible, because of the risks associated with movement or dislodgment (3,15). Since force and torque on the CI fixation exist under normal conditions found in the everyday life of a CI patient (removal of the external transmitter, stress during chewing or biting), a reasonable value for the stress on the fixation of the implant housing may be set by the typical force produced by the external transmitter during its removal. This typical force is between 0.3 and 1.0 N, depending on the distance between transmitter and receiver (typically 8 and 4 mm, respectively). The magnetic coupling between a subcutaneous internal CI magnet within the implant and a magnet in the external transmitter coil is an accepted means to guarantee sufficient transmission quality (1). The results obtained show that the different measured force components

remained within this acceptable limit. The switched gradients for spatial encoding are up to $\Delta B = 25$ mT/m, which is 100 times smaller than the static gradient on the entry of the bore. This produces a negligible force on the internal magnet ($F = 0.0027$ N) due to the switched gradients.

The stress on the fixation of the CI housing due to the torque can be calculated with the given implant geometry (Fig. 1). The torque on the CI translates into a force of, depending on the implant orientation, between 600 to 800 g trying to pull the edge of the implant from its proper position. For 1.5 T, this limit is exceeded by a factor of 8.

The associated risk for the patient arises from the possibility that the implant may turn and exert pressure on the brain. This risk is especially high with small children shortly after operation, where the bone underneath the implant is very thin or has been removed altogether. The thickness of the bone underneath the implant can be determined by computed tomography (CT).

With the stabilization experiment described, we tried to simulate the clinical situation of an implanted CI that is not adequately sutured to the bone. In general, the CI is fixed in a side-milled-out section of the temporal bone, and the stimulation electrode is placed into the cochlear. The electrodes are made of nonferromagnetic material. Apart from the deficits of the phantom used for the stabilization experiment (that the influence of reossification and the remaining temporal bone thickness could not be assessed), it was shown that improved stabilization of a CI that is not adequately sutured to the bone could be obtained by using a compression bandage for stabilization during MRI.

Still, the implant may, if not fixed well enough within its well, turn a few degrees from its proper position and possibly damage the proximal electrode leads by shear forces, resulting in a partial or total loss of implant functionality.

This raises several issues. First of all, technical means could be developed that reduce the torque to safe levels, eg, the use of magnet configurations or combinations that, due to compensation effects, generate only a very small residual torque. Another possibility would be the use of magnets that could be demagnetized before and remagnetized after MRI examination, in a safe manner. For the patient and the implant functionality, this is certainly to be preferred over the removal of the internal CI magnet (9). New surgical procedures could be developed as well, which could be demonstrated to hold the implant in place reliably, eg, the use of brackets fixed by bone screws. These considerations and the investigation of methods to determine the strength of a particular fixation will be the topic of further research.

What kind of solution can be offered in the mean time? Should CIs be banned from MRI examination altogether, or would it be possible to allow MRI examinations under special circumstances? No clear-cut answer can be given to this complex issue at present. A more cautious approach is certainly warranted since a wide variety of surgical techniques are being used for implant fixation (such as resolvable or non-resolvable sutures, ionomere cement fixation, stimulation of new bone formation, etc.) that differ in strength. There is also the additional factor of elapsed time since implantation. Up to now no reliable indicators have been available for the strength with which the implant is anchored to the bone.

On the other hand, circumstantial evidence from several cases indicates that C40 implants were sufficiently well fastened to withstand the torque induced (17). Therefore, an MRI examination should not be denied under specific circumstances, i.e., if the bone in the vicinity of the implant, as determined by CT imaging, is sufficiently thick, if evidence is available that adequate fixation was used for the implant, and if, as an additional safety measure, pressure bandages as shown in Fig. 6 are being used to restrict a possible movement of the implant. Certainly some assessment of the relative risks involved, i.e., possible electrode lead damage versus the risk of not providing the diagnostic capabilities of MRI, will have to be made.

CONCLUSIONS

It has been shown that most of the electromagnetic interferences between the CI (Med-El Combi 40/Combi 40+) and the 1.5 T scanner remain within acceptable limits. Nevertheless, force, torque, and fixation are issues that must be considered. The strong torque on the internal magnet represents a hazard for patients with this CI, especially if the implant is not adequately fixed to the bone. If an MRI investigation of a patient wearing the CI described is indispensable, the radiologist should perform a CT and, after some assessment of the relative risks involved, must judge whether an MR investigation for this patient is safe.

When an MRI investigation is necessary, external stabilization measures to reduce the angular displacement are strongly recommended and must be carefully prepared. The proper fixation of the implant housing must be ensured. Since the hazard remains of dislodging or hurting the patient due to the strong torque, indispensable MRI examinations should, at present, be allowed under restricted conditions only.

As a consequence of the great variety of equipment and procedures existing, it has not been possible to perform exhaustive tests on all available MR systems. Therefore additional experimental investigation in cooperation with the manufacturer may become necessary to determine the safety of the particular measurement procedure envisioned.

In any case, at present, we strongly advise consultation with the manufacturer to determine whether the particular MR procedure intended to be used with a CI patient is considered safe.

ACKNOWLEDGMENTS

Access to the MRI scanner was granted by the Department of Magnetic Resonance Tomography, University of Innsbruck, Austria, Department Head F. Aichner, MD.

REFERENCES

1. Dormer K, Richard G, Hough J, Nordquist R. The use of rare-earth magnet couplers in cochlear implants. Laryngoscope 1981;91:1812–1820.
2. Portnoy W, Matucci K. Cochlear implants as a contraindication to magnetic resonance imaging. Ann Otol Rhinol Otolaryngol 1991;100: 195–197.
3. Shellock F, Curtis J. MR imaging and biomedical implants, materials, and devices: an updated review. Radiology 1991;180:541–550.
4. Applebaum E, Valvassori G. Further studies on the effects of magnetic resonance fields on middle ear implants. Ann Otol Rhinol Laryngol 1990;99:801–804.
5. Kagetsu N, Litt A. Important considerations in measurement of attractive force on metallic implants in MR imagers. Radiology 1991;179:505–508.
6. Shellock F, Crues J. High-field-strength MR imaging and metallic biomedical implants: an ex vivo evaluation of deflection forces. AJR 1988;151:389–392.
7. Soulen R, Budinger T, Higgins C. Magnetic resonance imaging of prosthetic heart valves. Radiology 1985;154:705–707.
8. Pavlicek W, Geisinger M, Castle L, et al. The effects of nuclear magnetic resonance on patients with cardiac pacemakers. Radiology 1983;147:149–153.
9. Heller J, Brackmann D, Tucci D, Nyenhuis J, Chou C. Evaluation of MRI compatibility of the modified nucleus multichannel auditory brainstem and cochlear implants. Am J Otol 1996;17:724–729.
10. Portillo F, McCreery D, Waluch V, Mobley J, Nelson R. Effects of magnetic resonance imaging on auditory brainstem implant. In: Hochmair-Desoyer IJ, Hochmair E, editor. Advances in Cochlear Implants, Proceedings of the 3rd International Cochlear Implant Conference, April, 1993, Innsbruck, Austria; 1993. p 178–185.
11. Zierhofer C, Hochmair-Desoyer I, Hochmair E. Electronic design of a cochlear implant for multichannel high-rate pulsatile stimulation strategies. IEEE Trans Rehabil Eng 1995;3:112–116.
12. New P, Rosen B, Brady T, Buonanno F, et al. Potential hazards and artifacts of ferromagnetic and nonferromagnetic surgical and dental materials and devices in nuclear magnetic resonance imaging. Radiology 1983;147:139–148.
13. Wickersheim K, Sun M. Fluoroptic(thermometry. Med Electronics1987;Feb:84–91.
14. International standard—medical electrical equipment—Part 2: Particular requirements for the safety of magnetic resonance equipment for medical diagnosis. Geneva, Switzerland: IEC Publications, Geneva, Switzerland; 1995. p 48–49.
15. Shellock F. Biological effects and safety aspects of magnetic resonance imaging. Magn Reson Q 1989;5:243–261.
16. Food and Drug Administration. Guidance for content and review of a magnetic resonance diagnostic device 510(k) application. Silver Spring, MD: FDA; 1988.
17. Baumgartner W, Youssefzadeh S, Franz P, Gstõettner W. Magnetic resonance imaging in cochlear implanted patients. In: NYU Medical Center, Abstract Book of the Vth International Cochlear Implant Conference, New York City; 1997. p 23.